Variational Processing of Multimode Squeezed Light

Aviv Karnieli,[1,2,*,†] Paul-Alexis Mor,[1,*,‡] Charles Roques-Carmes,[1,*,§] Eran Lustig,[1,2]
Jamison Sloan,[1] Jelena Vučković,[1] David A.B. Miller,[1] and Shanhui Fan[1]

[1] *E. L. Ginzton Laboratory, Stanford University, 348 Via Pueblo, Stanford, California 94305, USA*
[2] *Andrew and Erna Viterbi Department of Electrical and Computer Engineering, Technion—Israel Institute of Technology, Haifa 32000, Israel*

(Received 20 September 2025; revised 14 January 2026; accepted 3 March 2026; published 20 April 2026)

Integrated multimode quantum optics is a promising platform for scalable continuous-variable quantum technologies leveraging multimode squeezing in both the spatial and spectral domains. However, on-chip measurement, routing and processing the relevant "supermodes" over which the squeezing resource is distributed still scales quadratically with the number of modes N, causing a rapid increase in photonic circuit size and number of required measurements. Here, we introduce a variational scheme, relying on self-configuring photonic networks (SCNs) that learn and extract the most-squeezed supermodes sequentially, reducing both the circuit size and the experimental overhead. Using homodyne measurement as a cost function, a sparse SCN discovers the $l \ll N$ most significant supermodes using $O(lN)$ physical elements and optimization steps. We analyze and numerically simulate these architectures for both real-space and frequency-domain implementations, showing a fidelity close to unity between the learned circuit and the supermode decomposition, even in the presence of optical losses and detection noise. In the frequency domain, we show that circuit size can be further reduced by using inverse-designed surrogate networks, which emulate the layers learned thus far. Using two different frequency encoding schemes—uniformly and nonuniformly spaced frequency bins—we reduce an entire network (learning all N supermodes) to $O(N)$ and even $O(1)$ modulated cavities. Our results point toward chip-scale, resource-efficient quantum processing units and demultiplexers for continuous variable processing in multimode quantum optics, with applications ranging from quantum communication, metrology, and computation.

DOI: 10.1103/mcmq-qf4p

I. INTRODUCTION

Recent years have seen a surge of interest in the field of multimode quantum optics with squeezed light [1–14], with many applications for quantum technology [2–5,12,13,15–19], fundamental studies of light-matter interactions [20,21], and nonlinear dynamics of quantum noise [22–24]. One of the main drivers for the recent progress has been the promise of realizing high levels of squeezing on chip [12,25–33], owing to developments of low-loss, nonlinear integrated platforms for photonics. These are especially exciting for quantum optical applications employing squeezed states, ranging from quantum communication [3,4,19,34], continuous-variable quantum computation [2,12,13,16,18,35,36], and distributed quantum sensing [15,17].

Squeezing has become an extremely important quantum resource; however, its measurement often requires complex tomography over multiple degrees of freedom. Indeed, squeezing generated by many sources is often broadband and dispersed among multiple modes, such as spatial, spectral, and temporal bins, forming so-called squeezed "supermodes" [1,2]. Harvesting the squeezing resource—e.g., for use in quantum sensing and metrology [15,17]—entails the discovery of the exact superposition of modes the state is in. Moreover, multimode squeezed states are increasingly employed as a platform for multiplexed quantum information encoding, enabling quantum information to be distributed and processed across a large number of modes [2,12,13,16,18,35,36]. Multiplexing of continuous-variable quantum information has emerged as a key enabler for scalable photonic quantum technologies. Multiplexed squeezed states underpin Gaussian boson sampling experiments [12], quantum computation

---

[*] These authors contributed equally to this work.
[†] Contact author: karnieli@technion.ac.il
[‡] Contact author: paul-alexis.mor@mines.org
[§] Contact author: chrc@stanford.edu

with large-scale cluster states [2,36,39], and multiuser continuous-variable quantum networking [40–42]. However, the rapid increase in the mode number poses a big challenge in hardware. For this reason, it is imperative to have experimental methods for processing multimode squeezed states in a hardware-efficient manner.

Current measurement techniques [3,4,7–10,43–45] generally rely on direct quantum state tomography using homodyne detection (HD) [1] with a local oscillator (LO) shaped into arbitrary superpositions of modes using, e.g., off-chip pulse shapers [3,4,10], spatial light modulators and masks [7,43], or nonlinear interferometers [8,30,44]; other techniques employ direct measurement of spatial [9,45] or spectral [46] intensity correlations. On-chip implementations [11,12,16,47–49], on the other hand, usually employ quantum processing units (QPUs) comprising programmable meshes of Mach-Zehnder interferometers (MZIs) [50–52] to implement a general unitary transformation on the basis of modes, followed by a measurement stage at the output. These architectures are particularly important if we wish not only to measure but also to generate, shape, and route squeezed supermodes for further quantum communication, computation, and sensing applications.

However, there remains a major challenge to scaling up multimode quantum information processing implemented on-chip. For quantum states encoded in N modes, QPUs require $O(N^2)$ physical elements to fully determine all the supermodes. Furthermore, unless simplifying assumptions can be made on the symmetry of supermodes [4,10],

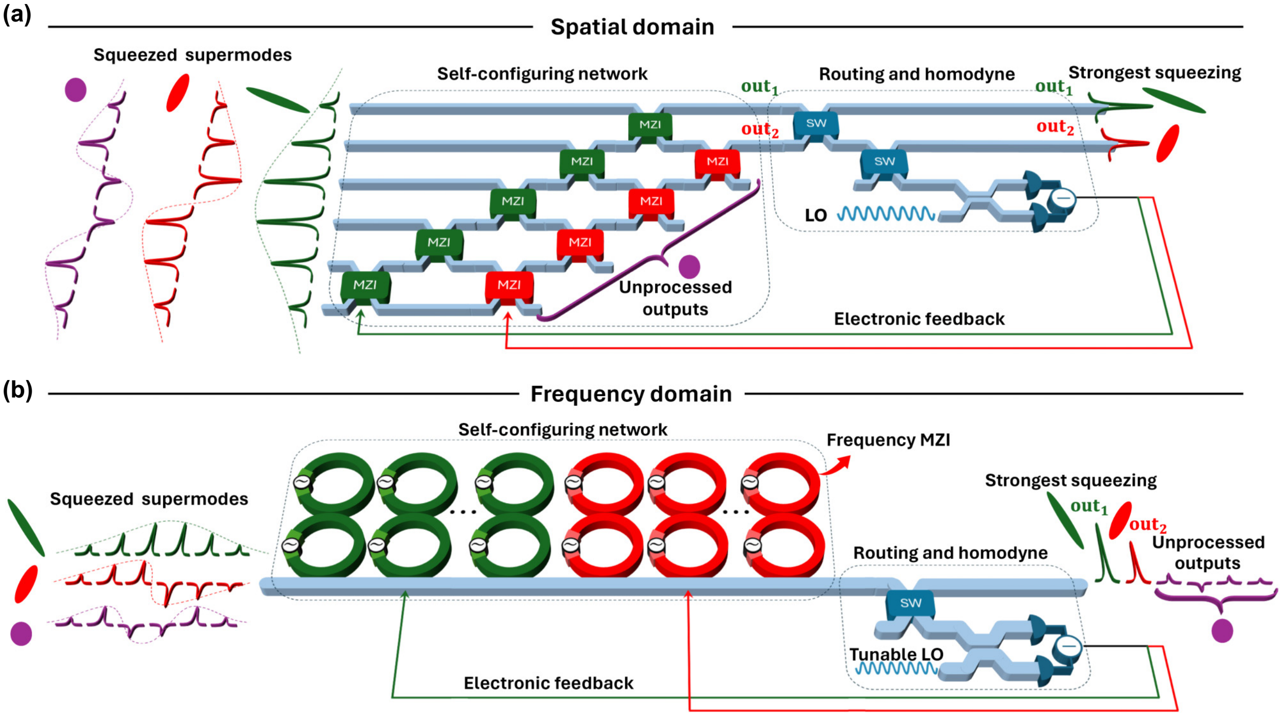

FIG. 1. Variational processing of multimode squeezed light using self-configuring optics. Squeezed supermodes are processed by a self-configuring network. The network comprises a mesh of Mach-Zehnder interferometers in a layered structure, where different layers are color-coded. Each layer has a single output port, while the rest of the ports are fed to the next layer. Output ports are routed through a layer of cross/bar switches to the homodyne measurement stage with a continuous-wave local oscillator. Consecutive learning of each layer's Mach-Zehnder interferometer parameters is performed by optimizing over the homodyne signal (as in Fig. 2), while parameters are updated with electronic feedback. Once learning has converged, the output port of layer i is guaranteed to carry the ith most squeezed supermode, and the Mach-Zehnder interferometer parameters of layer i correspond to the expansion coefficients of supermode i. For sparse networks (where the number of layers is smaller than the number of modes), the remaining unprocessed outputs carry the lowest squeezing and span a subspace orthogonal to the discovered supermodes. If one wishes to find the first $l \ll N$ dominant supermodes, then the number of physical elements required is $O(lN)$. Here, two out of six modes are chosen to demonstrate the network's ability to find the first two most squeezed supermodes. (a) Implementation in the spatial domain. Modes are encoded in the path degree of freedom (e.g., waveguide number), and Mach-Zehnder interferometer meshes are physically implemented on chip. (b) Implementation in the frequency domain. Modes are now encoded using frequency bins. With the equivalent of a frequency-domain Mach-Zehnder interferometer scattering element coupled to a waveguide [37] (see derivation in the Supplemental Material, Section S12D [38]), meshes are implemented in synthetic dimension, and the continuous-wave local oscillator can be tuned to a specific frequency bin being measured. We note that in the frequency domain architecture, the squeezed supermodes are now routed to different frequency bins, to be separated and processed independently.

one generally needs to tomographically reconstruct the entire state to find even a single supermode, which requires $O(N^2)$ measurement steps in the worst case. This quadratic scaling constrains not only spatial meshes of integrated MZIs [52–54], but also integrated QPUs implemented in the frequency domain [11,55] using spectral beam splitters [37].

Here, we propose alternative schemes for measuring, processing, and decomposing multimode squeezed states in the spatial and spectral domains, relying on variational principles. Our method employs self-configuring networks (SCNs) [56–63], a layered architecture for photonic circuits that allows automated sequential decomposition of an optical input into its eigenmodes. We show that by maximizing over a homodyne detection signal at the output of each layer of the SCN (see Fig. 1), with respect to the MZI variables of the layers, we can sequentially find the most squeezed supermodes in the system, while routing their respective squeezing into corresponding output ports. This permits favorable scalings with the number of modes, in both the quantity of on-chip physical elements and the number of iterations required for finding the dominant supermodes. Note, too, that this separation into supermodes by self-configuration does not rely on any calibration of the MZIs nor on their perfection. We then propose and analyze different architectures realizing these variational processors in both the spatial and the spectral domains, where the use of the synthetic frequency dimension [64] enables us to compress the spatial footprint of the *entire* circuit even further down to $O(N)$ and even $O(1)$ physical elements. Our approach paves the way towards scalable on-chip processing of high-dimensional squeezed states, with applications to quantum communication, sensing, and computation.

The paper is organized as follows. In Sec. II, we introduce the theoretical background on the squeezed supermode decomposition (the Bloch-Messiah decomposition), introduce the self-configuring architectures in both the spatial and spectral domains for efficiently learning the supermodes, and discuss and numerically analyze the variational algorithm used for the learning procedure. Based on these foundations, in Sec. III, we introduce more advanced self-configuring architectures in the frequency domain, which utilize the concept of surrogate networks that can further improve scalability. We then discuss in Sec. IV the experimental considerations for implementing our schemes and conclude with a discussion of future outlook in Sec. V.

II. VARIATIONAL PROCESSING OF MULTIMODE SQUEEZING

A. The Bloch-Messiah decomposition

We denote the quadratures of mode i as $x_i = a_i + a_i^\dagger$ and $p_i = (a_i - a_i^\dagger)/i$, where a_i is the photon annihilation operator. In a multimode state of N modes, these quadratures form a $2N$-long quadrature vector $\vec{q} = (x_1, x_2, \ldots, x_N, p_1, p_2, \ldots, p_N)$. The covariance matrix is given by the $2N$-by-$2N$, positive semidefinite and symmetric matrix

$$\Gamma = \frac{1}{2}\left\langle \delta\vec{q}\delta\vec{q}^T + (\delta\vec{q}\delta\vec{q}^T)^T \right\rangle , \qquad (1)$$

where $\delta\vec{q} = \vec{q} - \langle\vec{q}\rangle$. Processing multimode squeezed states then involves the measurement and subsequent decomposition of the covariance matrix, which encodes the entire information about the squeezed supermodes. Owing to the Bloch-Messiah decomposition (BMD) [1, 65], and in the presence of mode-independent photon loss, we are able to decompose the covariance matrix into a diagonal form via

$$\Gamma = (1-p)OK^2O^T + pI, \qquad (2)$$

where $O = [\mathrm{Re}U, -\mathrm{Im}U; \mathrm{Im}U, \mathrm{Re}U]$ is a $2N$-by-$2N$ real orthogonal matrix corresponding to a general N-by-N unitary mode mixing transformation U, $K = \mathrm{diag}(e^{r_1}, e^{r_2}, \ldots, e^{r_N}, e^{-r_1}, e^{-r_2}, \ldots, e^{-r_N})$ is a diagonal squeezer, with r_j denoting the jth squeeze parameter, I denotes the identity matrix, and p is the photon loss probability. Once the BMD of Eq. (2) is known, the complex coefficients of the ith supermode ($i = 1, \ldots, N$) can be inferred from the ith row of the orthogonal matrix O, and the amount of antisqueezing (respectively, squeezing) carried by this supermode can be read from the ith (respectively, $i + N$th) diagonal element of Γ_D. For a more comprehensive overview of the covariance matrix, symplectic transformations, and the BMD [1], see the Supplemental Material, Sections S1A and B [38]. The case of mode-dependent losses is dealt with in the Supplemental Material, Section S2E [38].

B. Self-configuring architecture in the spatial domain

For a highly multimode system, a desirable aspect of a device implementing the BMD is to not only reconstruct and measure the most squeezed supermodes, but also *routing* their respective squeezed quadratures into different output ports for further use. We will now show, using self-configuring architectures, how this procedure can be performed sequentially and automatically, where the photonic circuit discovers the most squeezed supermodes first. We do this for both the spatial (Fig. 1a) and the frequency [Fig. 1(b)] domains, as discussed below.

The proposed self-configuring architecture for implementing our variational processors of multimode squeezed states in the spatial domain is depicted in Fig. 1(a). The spatial bins are encoded in waveguide modes, and the photonic circuit is implemented through a mesh of MZIs. Each

MZI in the spatial domain comprises two 50/50 beamsplitters and two electrically controllable phase shifters (e.g., using thermo-optical control), phases of which we denote by θ_j and φ_j for the jth MZI. Self-configuring networks [52,56,57] comprise a cascade of layers of such MZI elements, with a specific topology: every input port has exactly one path through MZI blocks to the output port of the layer [57]. Examples include diagonal layers [depicted in Fig. 1(a)] as well as binary tree layers [57] and combinations thereof. Recently, such networks have been proposed [59,60] and experimentally demonstrated [58] to sequentially find eigenstates of classical communication channels [58], partially coherent light [59,66], and Schmidt modes of entangled photon pairs [60]. Unlike previous works, here we propose to employ self-configuring networks for the processing of multimode squeezed states, where the cost function for optimization is based on homodyne measurements. We make use of a variational principle to allow the network to automatically and sequentially learn the most significant supermodes and route them to separate output ports. This concept will provide the foundation for the more advanced architectures proposed later in the paper.

The input squeezed light comprises unknown supermodes [green, red, and magenta envelopes in Fig. 1(a)], dispersed over a discrete set of waveguide modes. The input state enters a self-configuring network: in this example, the number of bins is 6 whereas the network consists of two diagonal layers of MZIs. The output of each layer is the top right port in the spatial implementation [Fig. 1(a)]. After propagating through the network, the output port of layer 1 [denoted as out$_1$ in Fig. 1(a)] is routed to a homodyne measurement stage using selection switches, comprising MZI elements set to either totally transmit ("bar") or reflect ("cross") the input. The homodyne measurement is optimized (as will be described below) with respect to the MZI parameters of layer 1 until convergence, where electronic feedback is used to update the layer parameters.

Once the learning of the first layer has converged, the light in output port 1 is guaranteed to carry the squeezed quadratures of the most squeezed supermode, as explained below. The process can now be repeated to learn the second layer, cascaded to the first, where the parameters of layer 1 remain fixed. The output of the second layer will then carry the squeezed quadratures of the second-most squeezed supermode. If the network is sparse (the number of layers l smaller than the number of modes N, as in the example in Fig. 1), then all spatial modes orthogonal to the first l supermodes will remain unprocessed and routed to unused output ports. A key advantage made possible by the self-configuring architecture is, therefore, its ability to harvest the strongest squeezing resource encoded in the first l supermodes using sparse photonic circuits consisting of $O(lN)$ physical elements.

C. Self-configuring architecture in the frequency domain

We propose a similar architecture for self-configuring networks in the frequency domain, as depicted in Fig. 1(b). The input light travels in a single spatial mode in a waveguide and processed via scattering off electro-optically modulated micro-ring cavities side-coupled to the waveguide. The modes are encoded in frequency bins, which correspond to the resonance frequencies of the integrated ring resonators used to generate the squeezed light [31,32]. In the spectral implementation, the photonic circuits are built from units of integrated frequency-bin MZIs [37,55], each comprising two modulated rings that can selectively couple pairs of frequency bins through a scattering process [37,55] [see Fig. 1(b)]. The derivation of the unitary 2 × 2 MZI transformation is derived in the Supplemental Material, Section S1D [38]. As in the spatial domain, the jth frequency-domain MZI is controllable by two degrees of freedom θ_j and φ_j which correspond to the amplitude and phase of the electro-optic modulation of the MZI. Such integrated frequency-domain MZIs have been recently demonstrated experimentally [37]. Their operation principle relies on a mode splitting between two coupled ring cavities [37], where the splitting should correspond to the frequency-bin spacing of the input (e.g., the free spectral range (FSR) of the cavity generating the squeezed light).

The self-configuring layers are then built by cascading frequency-domain MZIs, as depicted in Fig. 1(b) for a diagonal layer, where the jth MZI couples the jth and $j+1$-st frequency bins. An input multimode squeezed light enters the network and scatters off the self-configuring network, and the optimization is performed by routing the entire output to the homodyne stage. To learn the first layer, a frequency-tunable continuous-wave (CW) LO is set to the first (e.g., lowest) frequency bin, corresponding to the output port of the first layer (and, whenever frequency bin j is optimized on, the LO frequency can be tuned to ω_j). The output is then optimized according to the protocol discussed below, and electronic feedback is used to update the layer parameters.

We note that whenever considering modes encoded in the frequency domain, the modes are not strictly discrete. In fact, the quadratures can also vary as a function of a frequency detuning ω relative to the center frequency of the ith frequency bin, such that $x_i(\omega) = a_i(\omega) + a_i^\dagger(-\omega)$ and $p_i(\omega) = (a_i(\omega) - a_i^\dagger(-\omega))/i$. These are in fact non-Hermitian operators that form a complex-valued covariance matrix $\Gamma(\omega)$, supporting morphing supermodes [11,67] that vary nonuniformly with ω. In the ensuing analysis, unless stated otherwise, we shall make two assumptions: first, we consider a region of ω smaller than the squeezing bandwidth around each resonance, thus effectively analyzing the decomposition of the real-valued covariance matrix $\Gamma \equiv \Gamma(0)$. Second, scattering elements that we use for optical processing in the frequency domain (such as cavities side-coupled to a waveguide) have a larger bandwidth around each resonance compared to the squeezing bandwidth of the quantum light. A unitary operator $U(\omega)$ associated with such elements acts approximately independent of ω within the relevant spectral range, and we can thus simplify $U = U(0)$. A full frequency-dependent treatment of our model is detailed in the Supplemental Material, Sections S1C–E [38], and the implications of bandwidth mismatch between the squeezing and scattering elements are discussed in the Supplemental Material, Section S3C [38].

D. Variational optimization using homodyne measurements

We now detail the variational optimization procedure the network uses to learn the parameters of each self-configuring layer using homodyne measurements. Homodyne detection is a fundamental tool for characterizing quantum states of light in phase space [1,68] and was recently implemented on chip [28]. When a quantum light field under investigation interferes with a coherent state LO of amplitude α in a balanced beam splitter (BS), the intensities of the output ports of the BS are measured using photodetectors, and their difference measures the operator $N_{-}(\phi) = 2|\alpha|(\cos\phi x + \sin\phi p) \equiv 2|\alpha| x_{\phi}$ where ϕ is the controllable phase of the LO. For Gaussian states it suffices to measure the first two moments of $N_{-}(\phi)$: Measuring $\langle N_{-}(\phi)\rangle$ reveals $\langle x_{\phi}\rangle$, while measuring the variance of $N_{-}(\phi)$ gives us the variance in the quadrature x_{ϕ}, or $\langle \delta x_{\phi}^2\rangle = \langle x_{\phi}^2\rangle - \langle x_{\phi}\rangle^2$. When the self-configuring network is learning its ith layer, the homodyne measurement is performed over the ith output port of the photonic circuit [ports out$_i$ in Figs. 1(a) and 1(b)], implementing a unitary U_c (correspondingly, an orthogonal transformation O_c), and we have that (see the Supplemental Material, Sections S2A and B for derivation [38])

$$\langle \delta x_{\phi,i}^2\rangle = \cos^2\phi \left[O_c\Gamma O_c^T\right]_{i,i} + \sin 2\phi \left[O_c\Gamma O_c^T\right]_{i,i+N} + \sin^2\phi \left[O_c\Gamma O_c^T\right]_{i+N,i+N}. \tag{3}$$

Note that Eq. (3) covers the full interferogram of quadrature variances for all ϕ. From the homodyne interferogram as a function of ϕ we can then extract a cost function for learning the ith layer, in the form of the Rayleigh quotient (see the Supplemental Material, Sections S2A and B for derivation [38]),

$$\mathcal{C}[\vec{o}_c^{(i)}] = [O_c\Gamma O_c^T]_{i,i} = \frac{\vec{o}_c^{(i)T}\Gamma\vec{o}_c^{(i)}}{\vec{o}_c^{(i)T}\vec{o}_c^{(i)}}, \tag{4}$$

where $\vec{o}_c^{(i)}$ denotes the ith column of O_c. Experimentally, this quantity is found from the recorded homodyne interferogram by either a Fourier transform or a least-square fit to a sinusoidal function according to Eq. (3), as detailed in Section S2.B. We bring the right-hand side of Eq. (4) to the form of a Rayliegh quotient as part of the application of the variational theorem.

Using the variational theorem and the cascading property of the self-configuring network described above, we show in the Supplemental Material, Section S2A [38] that the maximum of the quantity in Eq. (4) corresponds to the ith largest eigenvalue of Γ in Eq. (1),

$$\begin{aligned} &\max_{\vec{o}_c^{(i)}}(\mathcal{C}[\vec{o}_c^{(i)}]) = (1-p)e^{2r_i} + p, \\ &\operatorname*{argmax}_{\vec{o}_c^{(i)}}(\mathcal{C}[\vec{o}_c^{(i)}]) = \vec{o}^{(i)}, \end{aligned} \tag{5}$$

with $r_1 \geq r_2 \geq \cdots \geq r_i \geq \cdots \geq r_N$ being the ordered squeezing parameters and $\vec{o}^{(i)}$ is the ith column of O^T. Equation (5) is a direct result of the variational theorem: the maximum of the Rayleigh quotient of Eq. (4) is the largest eigenvalue of Γ, and the argument maximizing this expression is its corresponding eigenvector. Namely, once layers $1, 2, \ldots, i-1$ have been learned, layer i will learn the expansion coefficients ($\vec{o}^{(i)}$) and squeeze parameter r_i of the ith most (anti)squeezed supermode. The network, therefore, discovers the supermodes in their order of significance. For a full circuit ($l = N$), once the entire self-configuring network has converged, the learned circuit transformation satisfies $O_c = O^T$ (up to a multiplication by a diagonal matrix of ± 1 from the left), such that $O_c\Gamma O_c^T = (1-p)K^2 + pI$ reduces to the diagonal form of Γ according to Eq. (2). For a sparse network ($l \ll N$), the circuit routes the l most squeezed supermodes to the outputs, in their order of significance, while the subspace of supermodes orthogonal to the discovered ones remains unprocessed (as depicted in Fig. 1).

Figure 2 shows a numerical example for learning an entire circuit for the case of $N = 10$ modes. In this example, which is valid for both the spatial and spectral implementations described in Fig. 1, the self-configuring layers are learned consecutively. The cost function of Eq. (4) is extracted from the homodyne interferogram of Fig. 2(a) [see Eq. (3) and the Supplemental Material, Section S2B [38]] and maximized. In our simulation, we assume a loss probability of $p = 0.1$ and model the detection noise due to a final acquisition time (see the Supplemental Material, Section S2C [38]). Optimization is performed using automatic differentiation and a variant of stochastic gradient descent [69] (see the Supplemental Material, Section [38]).

A formal proof of convergence based on the properties of the Rayleigh quotient is provided in the Supplemental Material, Section S2D [38], where it was also shown numerically that each self-configuring layer converges in $O(N)$ iterations. This is evident from the steep convergence of the cost function in learning each of the layers in Fig. 2(b). For measuring the performance of the network in

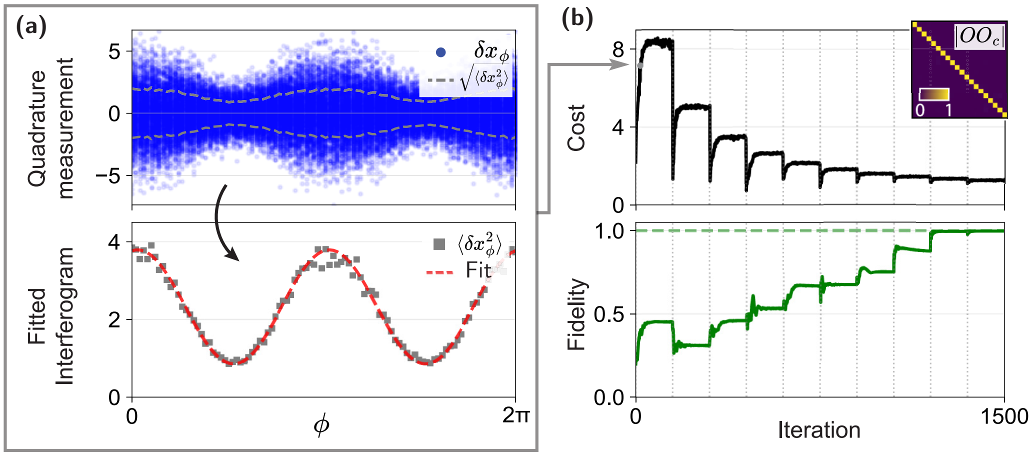

FIG. 2. Numerical simulation of variational learning of multimode squeezed light. (a) Simulated quadrature measurement, and the corresponding homodyne interferogram signal for the quadrature variance. The interferogram is fitted according to Eq. (3) and the cost function extracted according to the Supplemental Material, Section S2B [38]. (b) Plotted cost function [Eq. (4)] and overall Hilbert-Schmidt fidelity $\mathrm{Tr}|OO_C|/2N$ as a function of iteration number, where $|\cdot|$ denotes element-wise absolute value. The inset shows the product $|OO_C|$ to reflect the high fidelity between O_C and O^T.

recovering the correct BMD, we define a fidelity based on the Hilbert-Schmidt norm of matrices A, B of dimension d as $F = \mathrm{Tr}|A^T B|/d$, where $|\cdot|$ corresponds to an element-wise absolute value. As anticipated, the fidelity of the learned orthogonal transformation of the entire circuit O_C with BMD matrix O^T of the ground-truth converges to 1 after the entire network has been learned, as is also evident by the product $|OO_C|$ depicted in the inset of Fig. 2(b).

III. RESOURCE-EFFICIENT SELF-CONFIGURING FREQUENCY-DOMAIN CIRCUITS USING SURROGATE NETWORKS

A. Concept of surrogate network architecture

Frequency-domain quantum photonic circuits—employing synthetic dimensions in photonics [64]—are promising for decreasing the spatial footprint of on-chip circuits. As we show below, it is possible to reduce the number of cavities of a *full network* ($l = N$) to $O(N)$ and even $O(1)$, depending on the implementation. We will begin by describing the main concept and then detail two possible architectures to implement it in the frequency domain.

The idea is to physically separate the learning of layer i from the implementation of the previously learned layers $1, 2, \ldots, i-1$, as depicted in the block diagram of Fig. 3(a). That is, at each stage of learning, the ith supermode will be learned, and the previously learned supermode decomposition will be “stored” and implemented separately. The circuit that performs the learning is a *single* self-configuring layer of maximal length $N-1$ in the frequency domain, as discussed in the previous section. The implementation of the previously learned layers $1, 2, \ldots, i-1$ is done using a *surrogate network* situated right before the self-configuring layer that learns layer i. The surrogate network is an inverse-designed frequency-domain circuit—for example, the one proposed in Ref. [73]—which can be reconfigured after each layer has been learned.

Explicitly, let us consider the learning of the ith layer of the circuit (represented as a unitary $U^{(i)}$). Before the learning starts, the surrogate network is first inverse-designed to implement the unitary $U^{(i-1)}U^{(i-2)}\cdots U^{(1)}$ that has been learned thus fur, hence it routes the first $i-1$ supermodes to the first $i-1$ output frequency bins, while the remaining $i, i+1, \ldots, N$ frequency bins carry modes orthogonal to these supermodes. The learning self-configuring layer is then set to have its first $i-1$ MZIs idle (by turning off their modulation and have them act as 2×2 identity), while the optimization is performed over the parameters of the remaining $N-i$ MZIs, trying to maximize the cost function of the ith output frequency bin of Eq. (4). Once the learning of the ith layer $U^{(i)}$ has converged, the surrogate network will now be updated, by inverse design, to implement the updated unitary $U^{(i)}U^{(i-1)}\cdots U^{(1)}$, and the circuit will be ready to learn the $i+1$-st layer. We note that, while the inverse-design stage runs in only a few seconds on a standard PC, it may still become a limiting factor for the learning speed of the entire network, depending on homodyne trace acquisition times [74–76]. In these regimes, the computational overhead of inverse design becomes comparable to, or even exceeds, the experimental learning time of each layer.

We now proceed to propose implementations of this concept using two different architectures for frequency-domain quantum processors. The focus on the frequency-domain architectures stems from the ability to implement high-dimensional, full surrogate networks using fewer

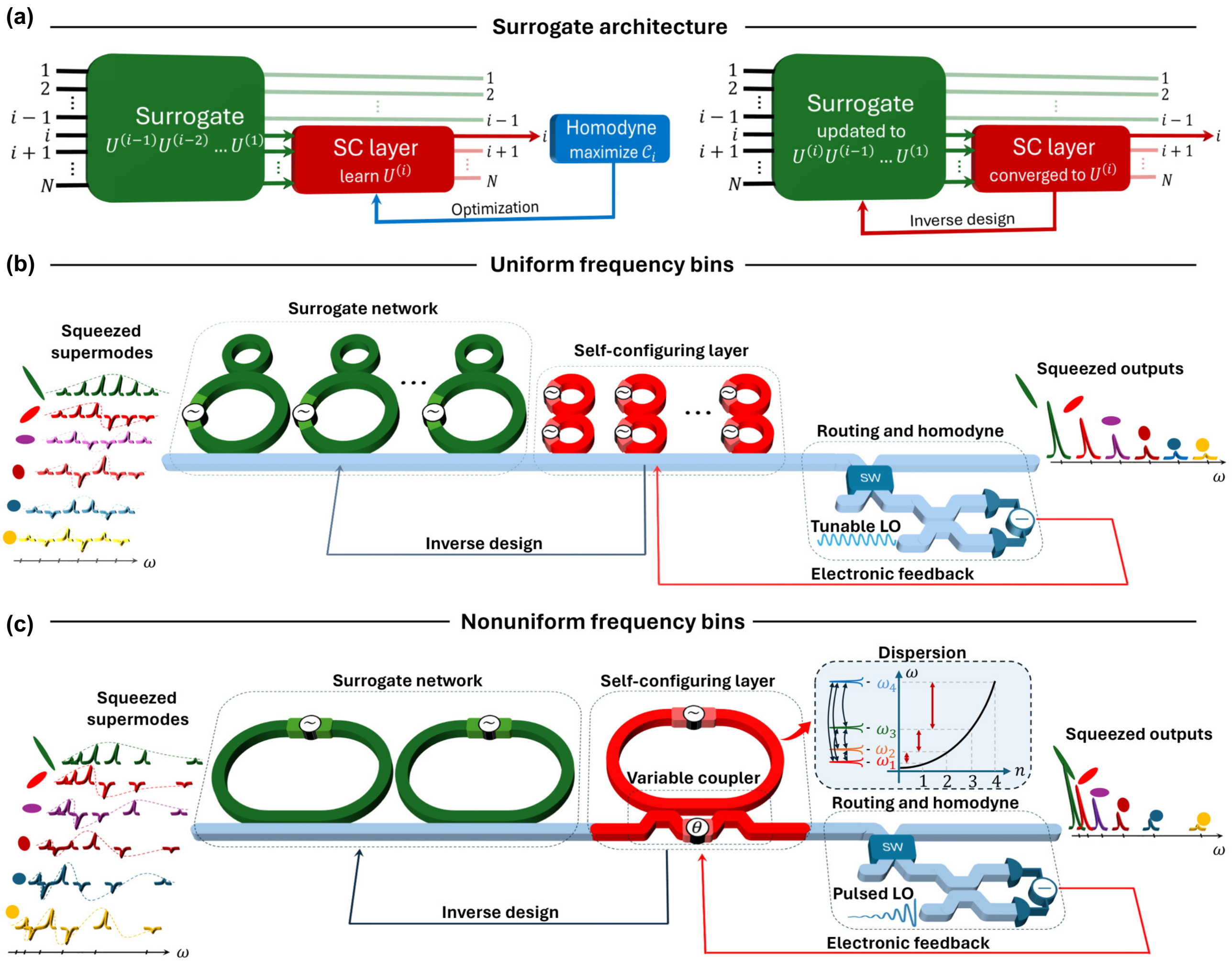

FIG. 3. Frequency domain self-configuring architectures with inverse-designed surrogate networks. (a) Block diagram of the circuit, which uses a single self-configuring layer for learning. After convergence, the surrogate network is inversely designed to implement the layers learned thus far, as detailed in the main text. (b) Implementation for uniform frequency bin encoding. The self-configuring layer and learning are implemented as in Fig. 1. The surrogate network comprises a cascade of N modulated microring cavities with frequency boundaries (realized by coupling each cavity to a smaller microring). Once a self-configuring layer has been learned, the surrogate network is respectively updated through inverse-design. Overall, the circuit requires $O(N)$ physical elements to implement an entire self-configuring network that discovers all N supermodes. (c) Implementation for nonuniform frequency bin encoding. Dispersive cavities with nonuniformly spaced resonances are used to process the squeezed supermodes, which are encoded on the same frequency ladder. The self-configuring layer is implemented using intracavity processing in a single modulated cavity with a variable Mach-Zehnder interferometer coupler to the waveguide [70–72]. Once the intracavity processing has concluded, the cavity field is unloaded into the waveguide and measured via homodyne using a pulsed local oscillator, as detailed in the main text and in the Supplemental Material, Section S3A [38]. The surrogate network, now comprising only two scattering cavities, is inversely designed accordingly. The circuit now requires $O(1)$ physical elements to implement an entire self-configuring network that discovers all N supermodes.

physical elements compared to the spatial domain implementation.

B. Surrogate networks using uniform frequency bins

We start by detailing the first architecture, depicted in Fig. 3(b). The self-configuring layer is implemented similarly to the ones in Fig. 1(b) and contains $N-1$ consecutive frequency-domain MZIs, which can be controllably driven to learn any layer $i = 1, \ldots, N$, based on feedback from a homodyne measurement on the frequency bin corresponding to the current layer's output.

The realization of the surrogate network, implementing the layers $1, \ldots, i-1$, is based on the proposal in Ref. [73]. Each of the cavities in the surrogate network is coupled to a smaller ring, forming a finite frequency boundary within which the inverse-designed circuit will operate. This is made possible by properly choosing the integer ratio p between the rings' FSR, such that every pth mode of the larger ring coincides with a mode of the smaller ring. Due to a strong coupling between the coinciding modes of the small and large rings, these modes split and are thus far detuned from any modulation at multiples of the larger ring's FSR, forming a frequency boundary.

Each cavity is electro-optically driven by a controllable external drive at multiples of the cavity's FSR Ω. The modulation signal spans multiple tones $\Omega_l = l\Omega$, each with a complex amplitude $\kappa_l \exp(i\phi_l)$, with $\kappa_{-l} = \kappa_l, \phi_{-l} = -\phi_l$, and $\kappa_0 = 0$. The modulation tones Ω_l thus couple modes ω_n with $\omega_{n\pm l}$ within the bounded frequency range. Assuming a constant photon loss rate (cavity linewidth γ_s), the unitary scattering matrix of the jth cavity of the surrogate network can be derived from input-output theory as (see the Supplemental Material, Section S1D [38] for the 2 × 2 case)

$$\mathrm{U}^{(j)} = \left(\mathrm{H}^{(j)} + i\frac{\gamma_s}{2}\right)\left(\mathrm{H}^{(j)} - i\frac{\gamma_s}{2}\right)^{-1}, \tag{6}$$

where the coupling matrix $\mathrm{H}^{(j)}_{mn} = \kappa^{(j)}_{m-n} \exp(i\phi^{(j)}_{m-n})$ is a Hermitian and Toeplitz matrix ($\mathrm{H}^{(j)}_{mn} = \mathrm{H}^{(j)}_{m-n}$) with zero diagonal (or at most constant, e.g., due to electro-optical rectification, self- and cross-phase modulation, in which case it can be calibrated into the cavity Hamiltonian). The coupling matrix thus has $2N - 2$ real degrees of freedom and hosts all-to-all couplings that are not mutually independent: all frequency bins spaced by the same integer multiple of the FSR have the same coupling. As was numerically proven in Ref. [73], cascading up to N such cavities with the proper inverse design of their coupling matrices allows for the implementation of arbitrary unitary transformations $U = U^{(N)}U^{(N-1)}\cdots U^{(1)}$ with close to unity fidelity. The learning procedure can thus be modeled numerically in an equivalent manner to Fig. 2. Remarkably, this architecture allows for an *entire* circuit to be implemented using exactly $2N$ cavities, instead of requiring $O(N^2)$ in the worst case.

C. Surrogate networks using nonuniform frequency bins

The second architecture we propose employs nonuniformly spaced frequency bins and dispersive cavities with matching resonances [Fig. 3(c)]. The learning of each self-configuring layer is performed using a single dispersive cavity. In addition, the cavity has a variable coupling to the waveguide (as implemented experimentally in Refs. [70–72]), and the learning is done using intracavity processing of the input light over a finite time. The surrogate network, on the other hand, is implemented using two additional scattering cavities. We assume that the multimode squeezed vacuum is a CW signal prepared on the same nonuniform frequency ladder, using, e.g., optical parametric oscillators (OPO) with a similar dispersion. Before we detail the learning protocol, we provide a few technical aspects on how the frequency-domain mode mixing behaves in this setting.

We consider a quadratic dispersion of the cavities such that the cavity resonances are given by $\omega_n = \omega_0 + n\Omega + n^2\Omega'$, as depicted in the inset of Fig. 3(c). The main conceptual difference is that the cavities are now driven by multiple tones that correspond to *all* possible couplings of frequencies ω_n and ω_m: $\Omega_{mn} = (m-n)\Omega + (m^2 - n^2)\Omega'$, each having a complex amplitude $\kappa_{mn}\exp(i\phi_{mn})$, with $\kappa_{mn} = \kappa_{nm}, \phi_{mn} = -\phi_{nm}$, and $\kappa_{mm} = 0$. Unlike the coupling matrix in the previous architecture, now we have all-to-all couplings that are mutually independent: every pair of frequencies can have a different complex coupling. However, this comes at the price that the resulting coupling matrix now hosts time-dependent detunings.

The time-dependent coupling matrix can be written as $\mathrm{H}(t) = \mathrm{H}_0 + \delta\mathrm{H}(t)$. Its time-independent part $\mathrm{H}_{0,mn} = \kappa_{mn}\exp(i\phi_{mn})$ corresponds to the desired couplings, forming a dense Hermitian matrix with zero diagonal ($\mathrm{H}_{0,mm} = 0$), and supports $N(N-1)$ real degrees of freedom. Its time-dependent part $\delta\mathrm{H}(t)$ contains all possible unintentional couplings with their corresponding detunings.

We define the smallest unintentional detuning in $\delta\mathrm{H}(t)$ as $\Delta \equiv \min_{mn\neq jk} |\Omega_{mn} - \Omega_{jk}|$. For a finite modulation time T, the unitary transformation generated by $\mathrm{H}(t)$ is $U_C = \mathcal{T}\exp\left[-i\int_0^T \mathrm{H}(t')dt'\right]$ with $\mathcal{T}$ denoting time ordering. In the limit where $T \gg 2\pi/\Delta \equiv T_0$, the time-dependent term $\delta\mathrm{H}(t)$ is fast oscillating and can be dropped, and U_C approaches the target unitary $U_{C,0} \equiv \exp(-i\mathrm{H}_0 T)$ (we further discuss the validity of this approximation below, as well as in the Supplemental Material, Sections S3C and D).

We consider the learning of the first supermode, such that the surrogate network [depicted in green in Fig. 3(c)] is turned off (not driven). The learning protocol of the self-configuring cavity [depicted in red in Fig. 3(c)] proceeds as follows and depicted in Fig. 4(a). First, the self-configuring cavity is initially empty and not driven. The coupler is then varied to a maximal external coupling to the waveguide, γ_e, such that the cavity is coupled to the CW squeezed vacuum input and steady state is reached. Then, the coupler is varied again to minimize the coupling with the waveguide (to a value smaller than the intrinsic loss rate γ_i). The CW input is turned off. Second, the cavity is then modulated for a finite modulation time $T \gg T_0$ with a target coupling matrix H_0, to implement a self-configuring layer O_C (corresponding to the target unitary $U_{C,0}$) that acts on the quantum light trapped in the cavity. Third, the coupler is reset to γ_e to dump the processed light into the waveguide. The resulting output signal takes a pulsed waveform. For this reason, to perform a homodyne measurement on the first frequency bin ω_0, the output signal is combined with a *pulsed* LO with the same temporal shape, $e^{-i\omega_0 t}\alpha_{LO}(t)$, unlike the frequency-domain architectures of Figs. 1(b) and 3(b), which employed a CW LO. We note that any added jitter to the pulsed LO, with a time scale t_{jitt}, attenuates the signal by $\exp(-\gamma_e t_{\text{jitt}}/2)$ and adds a vacuum noise of order $\gamma_e t_{\text{jitt}}$, and we therefore require $\gamma_e t_{\text{jitt}} \ll 1$. A similar requirement holds for the rise and fall times of the controls of the variable coupler. Each such measurement is performed for a single LO phase ϕ, and these steps are repeated until a full interferogram is acquired. For more details on this four-step learning procedure, see the Supplemental Material, Section S3A [38].

In the Supplemental Material, Section S3B [38], we show that for a maximal temporal overlap between the pulsed LO and the pulsed output signal, this entire protocol diagonalizes an effective covariance matrix given by

$$\Gamma_{\text{eff}} = e^{-\gamma_i T}\int d\omega \frac{1}{\pi}\frac{\gamma_e/2}{(\gamma_e/2)^2+\omega^2}\Gamma_{\text{in}}(\omega) + (1-e^{-\gamma_i T})\mathrm{I}, \tag{7}$$

where $\Gamma_{\text{in}}(\omega)$ is the frequency-dependent covariance matrix of the original CW input, and where $1-e^{-\gamma_i T}$ serves as the photon loss probability, producing a similar form to Eq. (2). In the Supplemental Material, Section S3B [38], we show that under our assumptions, Γ_{eff} shares the same supermodes and eigenvalue ordering as the input covariance matrix.

The surrogate network [depicted in green in Fig. 3(c)] comprises two scattering cavities with the same nonuniform dispersion, and we denote their linewidth as γ_s. Similarly to the self-configuring cavity, the scattering cavities are driven with time-dependent coupling matrices $\mathrm{H}^{(j)}(t)$ (with $j=1,2$), which, in the limit of $\gamma_s^{-1} \gg T_0$, approach the time-independent target matrices $\mathrm{H}_0^{(j)}$, and the surrogate network implements the target unitary $U_{C,0} = U_{C,0}^{(2)}U_{C,0}^{(1)}$, where the $U_{C,0}^{(j)}$ are given by Eq. (6) with $H^{(j)} = H_0^{(j)}$. Generalizing Ref. [73], in the Supplemental Material, Section S3C [38], we show that two such cavities are sufficient for the inverse design of an arbitrary unitary. Importantly, once the learning has been concluded, the surrogate network can scatter the incident CW input to a CW output, decomposed into the squeezed supermodes.

Figure 4(b) depicts a numerical simulation of the learning with nonuniform frequency bins, for $T = 10T_0$, $N = 10$ modes and 10% photon loss probability. For $\Gamma_{\text{in}}(\omega)$, we emulate a physical input prepared using an OPO squeezer followed by a mode-mixing cavity (for details, see the Supplemental Material, Section S3B [38]), and let the network learn Γ_{eff} of Eq. (7). In the considered regime, the supermodes are weakly morphing, and the circuit trained on Γ_{eff} learns the BMD of Γ_{in} with a fidelity of 99.58%, as shown in Fig. 4(b).

We note that imperfect fidelity between the target and actual unitaries U_C and $U_{C,0}$, of both the self-configuring and surrogate cavities, can affect the performance of the learning. We consider the process fidelity [77] between these two unitaries $F = |\mathrm{Tr}[U_C^\dagger U_{C,0}]|^2/N^2$ as a function of the relative modulation time T/T_0, the cavity's lifetime, and the mode number N, which sets a limit to the mode capacity of this architecture. In the Supplemental Material, Section S3D [38], we show that in general the process infidelity scales as $1-F \propto (T_0/T)^2$. Specifically, for the case of quadratic dispersion, we have $1-F \propto (N^2/\mathcal{F})^2$, where $\mathcal{F}$ denotes the cavity finesse. We confirm this scaling numerically for both the intracavity processing unitary and the surrogate scattering matrix, as depicted in Figs. 4(c) and 4(d), respectively.

IV. EXPERIMENTAL CONSIDERATIONS

One key challenge for the surrogate networks is the limited modulation bandwidth. This is because a surrogate network requires fully connected couplings across all frequency bins. State-of-the-art modulation rates are on the order of 100 GHz for both silicon modulators [78] and lithium-niobate electro-optic modulators [79]. Consequently, the number of accessible modes is constrained by the ratio of available bandwidth to the FSR, $N = \mathrm{BW}/\mathrm{FSR}$. Achieving networks with tens of modes therefore requires millimeter-scale racetrack resonators with FSRs of only a few gigahertz. Continued progress in modulator bandwidths, together with the use of resonators featuring longer round-trip lengths, could raise this limit to hundreds of modes.

For the nonuniform frequency-bin network, micro-ring resonators with controllable, nonuniform wavelength spacings can be realized through embedded photonic crystals [80,81] or through dispersion engineering via resonator geometry [82]. Racetrack resonators employing variable MZI couplers have already been demonstrated in Si [71, 83] and $\mathrm{SiO_2}$ [72], as well as in other material platforms, with reported finesse values exceeding $F = 100$ [72] in the telecom regime. A notable experimental challenge for future implementations will be pushing these finesse values higher, since the finesse $\mathcal{F}$, together with the number of modes N, sets an upper bound on the achievable infidelity $1-F$ [see Fig. 4(d)]: $1-F = (N^2/\pi\mathcal{F})^2$. We highlight that the analysis in this work used $\mathcal{F} = 1000$, whereas state-of-the-art microring resonators can reach $\mathcal{F} = 4 \times 10^4$ [84].

Regarding losses, the primary consideration for the device's operating regime is the requirement that the intrinsic loss γ_i be much smaller than the external coupling rate to the waveguide γ_e, i.e., $\gamma_e \gg \gamma_i$ (the strongly overcoupled regime). This condition ensures that the frequency-domain MZIs implement the correct unitary transformations [37]. Experimentally, the results in

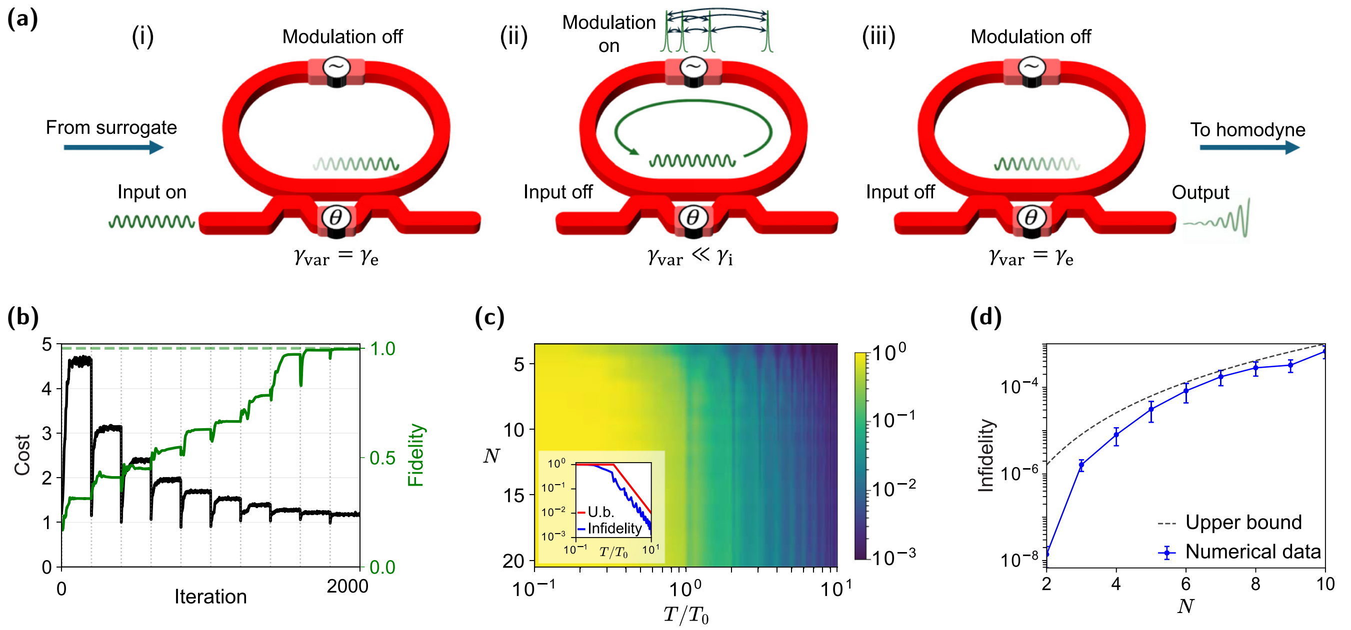

FIG. 4. Variational learning with nonuniform frequency bins. (a) Illustration of the intracavity learning procedure with the self-configuring cavity, as detailed in the main text. (b) Simulated learning of the effective covariance $\Gamma_{\rm eff}$ of Eq. (7) with $T = 10T_0$, and photon loss probability of 10% for a $N = 10$ system. The fidelity is calculated between the circuit O_C trained on $\Gamma_{\rm eff}$ and the BMD orthogonal matrix O of the original input covariance $\Gamma_{\rm in}(0)$. As the supermodes are weakly morphing, the two converge with a fidelity above 99%. For further details, see the Supplemental Material, Section S3B [38]. (c) Process infidelity $(1 - F)$ between the intracavity unitary $U_C = \mathcal{T}\exp\left[-i\int_0^T H(t')dt'\right]$ and the target unitary $U_{C,0} = \exp(-iTH_0)$, calculated numerically using trotterization, for different values of N and T/T_0. The inset shows the upper bound scaling $(T_0/T)^2$. (d) Process infidelity between the surrogate scattering unitary and the target unitary (calculated using the first-order Magnus expansion; error bars indicate standard deviation over 20 random target unitaries), for the case of quadratic dispersion and a finesse of $\mathcal{F} = 1000$, with the upper bound of $(N^2/\pi\mathcal{F})^2$. For more details, see the Supplemental Material, Sections S3C and D [38].

Ref. [37] already demonstrate that achieving $\gamma_e/\gamma_i \sim 30$ (corresponding to $Q_i \sim 10^6$) yields a frequency-shift ratio exceeding 99%. The on-chip loss of a frequency beam splitter scales as γ_i/γ_e [37], so for an array of N MZIs the total loss rate scales as $N\gamma_i/\gamma_e$, further emphasizing the importance of minimizing the number of physical MZIs in such designs. In the nonuniform frequency-bin architecture, the dominant effect of losses occurs during the intracavity processing stage, where based on Eq. (7) we require intrinsic losses satisfying $\gamma_i T \ll 1$.

V. DISCUSSION

We proposed and analyzed scalable on-chip architectures for processing multimode squeezed light. Using the notion of self-configuring networks, the photonic circuit can be sequentially optimized using homodyne measurements, which define an observable cost function that is then maximized. This method is a manifestation of the variational principle and enables us to learn and route the most squeezed supermodes of an input quantum state in their order of significance.

We discussed implementations in both the spatial and spectral domains using real and synthetic meshes of MZIs, allowing one to reduce the spatial footprint of such quantum processing units. Sparse networks—which discover the first $l \ll N$ dominant supermodes, where N is the number of modes, can be implemented using $O(lN)$ MZIs instead of $O(N^2)$ for a full network. In the frequency domain, the spatial footprint can be further reduced by employing inverse-designed surrogate networks that emulate the circuit learned thus far. Using two different frequency bin encoding schemes, we showed that the number of physical elements needed to implement an entire network (learning all N supermodes) can be reduced to $O(N)$ and even $O(1)$.

Our methods can inspire further development in multimode continuous-variable quantum technologies. An immediate application of our methods could be quantum-enhanced sensing across distributed channels. Once the supermodes are efficiently demultiplexed, the most squeezed outputs can be used as probes for different systems, as part of the distributed quantum sensing protocol [15,17]. Another avenue for quantum metrology is the use of the self-configuring methods for extracting the quantum Fisher information of the generated quantum light [85].

Our results could be especially exciting for the emerging field of frequency-bin quantum information processing

[55], where architectures for on-chip quantum processing units are currently being explored. We envision that self-configuring networks could also be useful for characterizing frequency-domain graph states, allowing scalable measurement of the entanglement witnesses (nullifiers) of these high-dimensional states [2], as well as for the measurement of bipartite [86] and multipartite [41,42,87] entanglement in continuous-variable quantum networks.

The ideas presented in this work could be extended to other encoding schemes. For example, it will be interesting to extend our protocols to time-bin and hybrid frequency-time bin encodings [57], which have been shown useful for scaling up high-dimensional entanglement [88,89]. Moreover, it can be useful to explore other nonuniform frequency bin encodings (such as the Golomb ruler [90]) to further improve circuit fidelity and mode capacity. Finally, our methods could generalize to other forms of multimode quantum noise measurement, such as in the photon-number basis and higher-order intensity correlations, for studying unique multimode and nonlinear quantum optical systems [23,24].

ACKNOWLEDGEMENTS

The authors acknowledge Kejie Fang and Toyota Research Institute of North America for useful discussions.

This work is supported by the Toyota Research Institute of North America, and by a MURI project from the U.S. Air Force Office of Scientific Research (Grant No. FA9550-21-1-0312). A.K. is supported by the VATAT-Quantum fellowship by the Israel Council for Higher Education; the Urbanek-Chodorow postdoctoral fellowship by the Department of Applied Physics at Stanford University; the Zuckerman STEM leadership postdoctoral program; and the Viterbi fellowship by the Technion. C.R.-C. is supported by a Stanford Science Fellowship. S.F. and D.A.B.M. acknowledge support by the Air Force Office of Scientific Research (AFOSR, Grant No. FA9550-21-1-0312). D.A.B.M. also acknowledges support by the Air Force Office of Scientific Research (AFOSR, Grant No. FA9550-23-1-0307). E.L., J.S., and J.V. were supported by the DARPA QUICC program and AFOSR Award No. FA9550-23-1-0248.

The authors are seeking patent protection for invention related to this work (US Patent Application 63/794810, Stanford University).

DATA AVAILABILITY

The data are not publicly available. The data are available from the authors upon reasonable request.

[1] C. Fabre and N. Treps, Modes and states in quantum optics, Rev. Mod. Phys. **92**, 035005 (2020).

[2] O. Pfister, Continuous-variable quantum computing in the quantum optical frequency comb, J. Phys. B: At., Mol. Opt. Phys. **53**, 012001 (2020).

[3] S. Armstrong, J.-F. Morizur, J. Janousek, B. Hage, N. Treps, P. K. Lam, and H.-A. Bachor, Programmable multimode quantum networks, Nat. Commun. **3**, 1026 (2012).

[4] J. Roslund, R. M. de Araújo, S. Jiang, C. Fabre, and N. Treps, Wavelength-multiplexed quantum networks with ultrafast frequency combs, Nat. Photonics **8**, 109 (2014).

[5] Y. Cai, J. Roslund, G. Ferrini, F. Arzani, X. Xu, C. Fabre, and N. Treps, Multimode entanglement in reconfigurable graph states using optical frequency combs, Nat. Commun. **8**, 15645 (2017).

[6] S. Gerke, J. Sperling, W. Vogel, Y. Cai, J. Roslund, N. Treps, and C. Fabre, Full multipartite entanglement of frequency-comb Gaussian states, Phys. Rev. Lett. **114**, 050501 (2015).

[7] C. S. Embrey, M. T. Turnbull, P. G. Petrov, and V. Boyer, Observation of localized multi-spatial-mode quadrature squeezing, Phys. Rev. X **5**, 031004 (2015).

[8] P. R. Sharapova, O. V. Tikhonova, S. Lemieux, R. W. Boyd, and M. V. Chekhova, Bright squeezed vacuum in a nonlinear interferometer: Frequency and temporal schmidt-mode description, Phys. Rev. A **97**, 053827 (2018).

[9] P. R. Sharapova, G. Frascella, M. Riabinin, A. M. Pérez, O. V. Tikhonova, S. Lemieux, R. W. Boyd, G. Leuchs, and M. V. Chekhova, Properties of bright squeezed vacuum at increasing brightness, Phys. Rev. Res. **2**, 013371 (2020).

[10] T. Kouadou, F. Sansavini, M. Ansquer, J. Henaff, N. Treps, and V. Parigi, Spectrally shaped and pulse-by-pulse multiplexed multimode squeezed states of light, APL Photonics **8**, 086113 (2023).

[11] B. Dioum, V. D'Auria, A. Zavatta, O. Pfister, and G. Patera, Universal quantum frequency comb measurements by spectral mode-matching, Opt. Quantum **2**, 413 (2024).

[12] J. M. Arrazola *et al.*, Quantum circuits with many photons on a programmable nanophotonic chip, Nature **591**, 54 (2021).

[13] L. S. Madsen, F. Laudenbach, M. F. Askarani, F. Rortais, T. Vincent, J. F. F. Bulmer, F. M. Miatto, L. Neuhaus, L. G. Helt, M. J. Collins, A. E. Lita, T. Gerrits, S. W. Nam, V. D. Vaidya, M. Menotti, I. Dhand, Z. Vernon, N. Quesada, and J. Lavoie, Quantum computational advantage with a programmable photonic processor, Nature **606**, 75 (2022).

[14] R. Li, B. An, N. Jiao, J. Liu, L. Chen, Y. Wang, and Y. Zheng, Bright squeezed light in the kilohertz frequency band, Light: Sci. Appl. **14**, 310 (2025).

[15] Q. Zhuang, Z. Zhang, and J. H. Shapiro, Distributed quantum sensing using continuous-variable multipartite entanglement, Phys. Rev. A **97**, 032329 (2018).

[16] F. Lenzini, J. Janousek, O. Thearle, M. Villa, B. Haylock, S. Kasture, L. Cui, H.-P. Phan, D. V. Dao, H. Yonezawa, P. K. Lam, E. H. Huntington, and M. Lobino, Integrated photonic platform for quantum information with continuous variables, Sci. Adv. **4**, eaat9331 (2018).

[17] X. Guo, C. R. Breum, J. Borregaard, S. Izumi, M. V. Larsen, T. Gehring, M. Christandl, J. S. Neergaard-Nielsen, and U. L. Andersen, Distributed quantum sensing in a continuous-variable entangled network, Nat. Phys. **16**, 281 (2020).

[18] G. Ferrini, J. P. Gazeau, T. Coudreau, C. Fabre, and N. Treps, Compact Gaussian quantum computation by multi-pixel homodyne detection, New J. Phys. **15**, 093015 (2013).

[19] F. Centrone, F. Grosshans, and V. Parigi, Cost and routing of continuous-variable quantum networks, Phys. Rev. A **108**, 042615 (2023).

[20] A. Gorlach, M. E. Tzur, M. Birk, M. Krüger, N. Rivera, O. Cohen, and I. Kaminer, High-harmonic generation driven by quantum light, Nat. Phys. **19**, 1689 (2023).

[21] J. Heimerl, A. Mikhaylov, S. Meier, H. Höllerer, I. Kaminer, M. Chekhova, and P. Hommelhoff, Multiphoton electron emission with non-classical light, Nat. Phys. **20**, 945 (2024).

[22] L. G. Wright, F. O. Wu, D. N. Christodoulides, and F. W. Wise, Physics of highly multimode nonlinear optical systems, Nat. Phys. **18**, 1018 (2022).

[23] N. Rivera, S. Z. Uddin, J. Sloan, and M. Soljačić, Ultra-broadband and passive stabilization of ultrafast light sources by quantum light injection, Nanophotonics **14**, 1857 (2025).

[24] S. Zia Uddin, N. Rivera, D. Seyler, J. Sloan, Y. Salamin, C. Roques-Carmes, S. Xu, M. Y. Sander, I. Kaminer, and M. Soljačić, Noise-immune quantum correlations of intense light, Nat. Photonics **19**, 751 (2025).

[25] A. Dutt, K. Luke, S. Manipatruni, A. L. Gaeta, P. Nussenzveig, and M. Lipson, On-chip optical squeezing, Phys. Rev. Appl. **3**, 044005 (2015).

[26] Y. Zhao, Y. Okawachi, J. K. Jang, X. Ji, M. Lipson, and A. L. Gaeta, Near-degenerate quadrature-squeezed vacuum generation on a silicon-nitride chip, Phys. Rev. Lett. **124**, 193601 (2020).

[27] Z. Yang, M. Jahanbozorgi, D. Jeong, S. Sun, O. Pfister, H. Lee, and X. Yi, A squeezed quantum microcomb on a chip, Nat. Commun. **12**, 4781 (2021).

[28] J. F. Tasker, J. Frazer, G. Ferranti, E. J. Allen, L. F. Brunel, S. Tanzilli, V. D'Auria, and J. C. F. Matthews, Silicon photonics interfaced with integrated electronics for 9 GHz measurement of squeezed light, Nat. Photonics **15**, 11 (2021).

[29] Y. Zhang, M. Menotti, K. Tan, V. D. Vaidya, D. H. Mahler, L. G. Helt, L. Zatti, M. Liscidini, B. Morrison, and Z. Vernon, Squeezed light from a nanophotonic molecule, Nat. Commun. **12**, 2233 (2021).

[30] R. Nehra, R. Sekine, L. Ledezma, Q. Guo, R. M. Gray, A. Roy, and A. Marandi, Few-cycle vacuum squeezing in nanophotonics, Science **377**, 1333 (2022).

[31] M. A. Guidry, D. M. Lukin, K. Y. Yang, and J. Vučković, Multimode squeezing in soliton crystal microcombs, Optica **10**, 694 (2023).

[32] E. Lustig, M. A. Guidry, D. M. Lukin, S. Fan, and J. Vuckovic, Quadrature-dependent lattice dynamics of dissipative microcombs, Nat. Photonics **19**, 1247 (2025).

[33] Y. Shen, P.-Y. Hsieh, D. Srinivasan, A. Henry, G. Moille, S. K. Sridhar, A. Restelli, Y.-C. Chang, K. Srinivasan, T. A. Smith, and A. Dutt, Highly squeezed nanophotonic quantum microcombs with broadband frequency tunability, arXiv:2505.03734.

[34] M. Sennary, J. Rivera-Dean, M. ElKabbash, V. Pervak, M. Lewenstein, and M. T. Hassan, Attosecond quantum uncertainty dynamics and ultrafast squeezed light for quantum communication, Light: Sci. Appl. **14**, 350 (2025).

[35] V. Cimini, M. M. Sohoni, F. Presutti, B. K. Malia, S.-Y. Ma, R. Yanagimoto, T. Wang, T. Onodera, L. G. Wright, and P. L. McMahon, Large-scale quantum reservoir computing using a Gaussian Boson Sampler, arXiv:2505.13695.

[36] Z. Wang, K. Li, Y. Wang, X. Zhou, Y. Cheng, B. Jing, F. Sun, J. Li, Z. Li, B. Wu, Q. Gong, Q. He, B.-B. Li, and Q.-F. Yang, Large-scale cluster quantum microcombs, Light: Sci. Appl. **14**, 164 (2025).

[37] Y. Hu, M. Yu, D. Zhu, N. Sinclair, A. Shams-Ansari, L. Shao, J. Holzgrafe, E. Puma, M. Zhang, and M. Lončar, On-chip electro-optic frequency shifters and beam splitters, Nature **599**, 587 (2021).

[38] See Supplemental Material at http://link.aps.org/supplemental/10.1103/mcmq-qf4p for background on the Bloch-Messiah and Williamson decomposition, sequential optimization algorithms for automatic Bloch-Messiah decomposition using homodyne detection and self-configuring optics, and model for optimization with non-uniform frequency bins, which also includes Refs. [91–94].

[39] M. V. Larsen, X. Guo, C. R. Breum, J. S. Neergaard-Nielsen, and U. L. Andersen, Deterministic generation of a two-dimensional cluster state, Science **366**, 369 (2019).

[40] C. Weedbrook, S. Pirandola, R. GarciaPatron, N. J. Cerf, T. C. Ralph, J. H. Shapiro, and S. Lloyd, Gaussian quantum information, Rev. Mod. Phys. **84**, 621 (2012).

[41] Y. Zhou, J. Yu, Z. Yan, X. Jia, J. Zhang, C. Xie, and K. Peng, Quantum secret sharing among four players using multipartite bound entanglement of an optical field, Phys. Rev. Lett. **121**, 150502 (2018).

[42] Y. Qin, J. Cheng, J. Ma, D. Zhao, Z. Yan, X. Jia, C. Xie, and K. Peng, Efficient and secure quantum secret sharing for eight users, Phys. Rev. Res. **6**, 033036 (2024).

[43] L. L. Volpe, S. De, T. Kouadou, D. Horoshko, M. I. Kolobov, C. Fabre, V. Parigi, and N. Treps, Multimode single-pass spatio-temporal squeezing, Opt. Express **28**, 12385 (2020).

[44] Y. Shaked, Y. Michael, R. Z. Vered, L. Bello, M. Rosenbluh, and A. Pe'er, Lifting the bandwidth limit of optical homodyne measurement with broadband parametric amplification, Nat. Commun. **9**, 609 (2018).

[45] M. Amooei, G. Kulkarni, J. Upham, and R. W. Boyd, Efficient characterization of spatial Schmidt modes of multiphoton entangled states produced from high-gain parametric down-conversion, Phys. Rev. A **111**, 023714 (2025).

[46] F. Presutti, L. G. Wright, S.-Y. Ma, T. Wang, B. K. Malia, T. Onodera, and P. L. McMahon, Highly multimode visible squeezed light with programmable spectral correlations through broadband up-conversion, arXiv:2401.06119.

[47] D. Barral, M. Walschaers, K. Bencheikh, V. Parigi, J. A. Levenson, N. Treps, and N. Belabas, Versatile photonic entanglement synthesizer in the spatial domain, Phys. Rev. Appl. **14**, 044025 (2020).

[48] H. H. Zhu, H. Sen Chen, T. Chen, Y. Li, S. B. Luo, M. F. Karim, X. S. Luo, F. Gao, Q. Li, H. Cai, L. K. Chin, L. C. Kwek, B. Nordén, X. D. Zhang, and A. Q. Liu, Large-scale photonic network with squeezed vacuum states for molecular vibronic spectroscopy, Nat. Commun. **15**, 6057 (2024).

[49] H. Aghaee Rad *et al.*, Scaling and networking a modular photonic quantum computer, Nature **638**, 912 (2025).

[50] N. C. Harris, J. Carolan, D. Bunandar, M. Prabhu, M. Hochberg, T. Baehr-Jones, M. L. Fanto, A. M. Smith, C. C. Tison, P. M. Alsing, and D. Englund, Linear programmable nanophotonic processors, Optica **5**, 1623 (2018).

[51] J. Wang, F. Sciarrino, A. Laing, and M. G. Thompson, Integrated photonic quantum technologies, Nat. Photonics **14**, 273 (2020).

[52] W. Bogaerts, D. Pérez, J. Capmany, D. A. B. Miller, J. Poon, D. Englund, F. Morichetti, and A. Melloni, Programmable photonic circuits, Nature **586**, 207 (2020).

[53] J. Wang, S. Paesani, Y. Ding, R. Santagati, P. Skrzypczyk, A. Salavrakos, J. Tura, R. Augusiak, L. Mančinska, D. Bacco, D. Bonneau, J. W. Silverstone, Q. Gong, A. Acín, K. Rottwitt, L. K. Oxenløwe, J. L. O'Brien, A. Laing, and M. G. Thompson, Multidimensional quantum entanglement with large-scale integrated optics, Science **360**, 285 (2018).

[54] J. Wang, F. Sciarrino, A. Laing, and M. G. Thompson, Integrated photonic quantum technologies, Nat. Photonics **14**, 273 (2020).

[55] H.-H. Lu, M. Liscidini, A. L. Gaeta, A. M. Weiner, and J. M. Lukens, Frequency-bin photonic quantum information, Optica **10**, 1655 (2023).

[56] D. A. B. Miller, Self-configuring universal linear optical component [Invited], Photonics Res. **1**, 1 (2013).

[57] D. A. B. Miller, Analyzing and generating multimode optical fields using self-configuring networks, Optica **7**, 794 (2020).

[58] S. SeyedinNavadeh, M. Milanizadeh, F. Zanetto, G. Ferrari, M. Sampietro, M. Sorel, D. A. B. Miller, A. Melloni, and F. Morichetti, Determining the optimal communication channels of arbitrary optical systems using integrated photonic processors, Nat. Photonics **18**, 149 (2024).

[59] C. Roques-Carmes, S. Fan, and D. A. B. Miller, Measuring, processing, and generating partially coherent light with self-configuring optics, Light: Sci. Appl. **13**, 260 (2024).

[60] C. Roques-Carmes, A. Karnieli, D. A. B. Miller, and S. Fan, Automated modal analysis of entanglement with bipartite self-configuring optics, ACS Photonics **12**, 3285 (2025).

[61] R. Hamerly, S. Bandyopadhyay, and D. Englund, Stability of self-configuring large multiport interferometers, Phys. Rev. Appl. **18**, 024018 (2022).

[62] R. Hamerly, S. Bandyopadhyay, and D. Englund, Accurate self-configuration of rectangular multiport interferometers, Phys. Rev. Appl. **18**, 024019 (2022).

[63] S. Bandyopadhyay, R. Hamerly, and D. Englund, Hardware error correction for programmable photonics, Optica **8**, 1247 (2021).

[64] L. Yuan, Q. Lin, M. Xiao, and S. Fan, Synthetic dimension in photonics, Optica **5**, 1396 (2018).

[65] S. L. Braunstein, Squeezing as an irreducible resource, Phys. Rev. A **71**, 055801 (2005).

[66] Mor *et al.*, Separating partially coherent light, arXiv:2603.15517

[67] E. Gouzien, S. Tanzilli, V. D'Auria, and G. Patera, Morphing supermodes: A full characterization for enabling multimode quantum optics, Phys. Rev. Lett. **125**, 103601 (2020).

[68] A. I. Lvovsky and M. G. Raymer, Continuous-variable optical quantum-state tomography, Rev. Mod. Phys. **81**, 299 (2009).

[69] D. P. Kingma and J. Ba, Adam: A method for stochastic optimization, arXiv:1412.6980.

[70] W. M. J. Green, R. K. Lee, G. A. DeRose, A. Scherer, and A. Yariv, Hybrid InGaAsP-InP Mach-Zehnder racetrack resonator for thermooptic switching and coupling control, Opt. Express **13**, 1651 (2005).

[71] R. Yang, L. Zhou, H. Zhu, and J. Chen, Low-voltage high-speed coupling modulation in silicon racetrack ring resonators, Opt. Express **23**, 28993 (2015).

[72] Y.-X. Yin, X.-P. Zhang, X.-J. Yin, Y. Li, X.-R. Xu, J.-M. An, Y.-D. Wu, X.-P. Liu, and D.-M. Zhang, High-Q-factor tunable silica-based microring resonators, Photonics **8**, 256 (2021).

[73] S. Buddhiraju, A. Dutt, M. Minkov, I. A. D. Williamson, and S. Fan, Arbitrary linear transformations for photons in the frequency synthetic dimension, Nat. Commun. **12**, 2401 (2021).

[74] G. Breitenbach, S. Schiller, and J. Mlynek, Measurement of the quantum states of squeezed light, Nature **387**, 471 (1997).

[75] M. Mehmet, S. Ast, T. Eberle, S. Steinlechner, H. Vahlbruch, and R. Schnabel, Squeezed light at 1550 nm with a quantum noise reduction of 12.3 dB, Opt. Express **19**, 25763 (2011).

[76] H. Vahlbruch, M. Mehmet, K. Danzmann, and R. Schnabel, Detection of 15 dB squeezed states of light and their application for the absolute calibration of photoelectric quantum efficiency, Phys. Rev. Lett. **117**, 110801 (2016).

[77] M. A. Nielsen, A simple formula for the average gate fidelity of a quantum dynamical operation, Phys. Lett. A **303**, 249 (2002).

[78] C. Han, Z. Zheng, H. Shu, M. Jin, J. Qin, R. Chen, Y. Tao, B. Shen, B. Bai, F. Yang, Y. Wang, H. Wang, F. Wang, Z. Zhang, S. Yu, C. Peng, and X. Wang, Slow-light silicon modulator with 110-GHz bandwidth, Sci. Adv. **9**, eadi5339 (2023).

[79] P. O. Weigel, J. Zhao, K. Fang, H. Al-Rubaye, D. Trotter, D. Hood, J. Mudrick, C. Dallo, A. T. Pomerene, A. L. Starbuck, C. T. DeRose, A. L. Lentine, G. Rebeiz, and S. Mookherjea, Bonded thin film lithium niobate modulator on a silicon photonics platform exceeding 100 GHz 3-dB electrical modulation bandwidth, Opt. Express **26**, 23728 (2018).

[80] D. Goldring, U. Levy, and D. Mendlovic, Highly dispersive micro-ring resonator based on one dimensional photonic crystal waveguide design and analysis, Opt. Express **15**, 3156 (2007).

[81] S. M. Lo, S. Hu, G. Gaur, Y. Kostoulas, S. M. Weiss, and P. M. Fauchet, Photonic crystal microring resonator for label-free biosensing, Opt. Express **25**, 7046 (2017).

[82] K. Y. Yang, K. Beha, D. C. Cole, X. Yi, P. Del'Haye, H. Lee, J. Li, D. Y. Oh, S. A. Diddams, S. B. Papp, and K. J. Vahala, Broadband dispersion-engineered microresonator on a chip, Nat. Photonics **10**, 316 (2016).

[83] W. D. Sacher, W. M. J. Green, S. Assefa, T. Barwicz, H. Pan, S. M. Shank, Y. A. Vlasov, and J. K. S. Poon, Coupling

modulation of microrings at rates beyond the linewidth limit, Opt. Express **21**, 9722 (2013).

[84] W. Jin, Q.-F. Yang, L. Chang, B. Shen, H. Wang, M. A. Leal, L. Wu, M. Gao, A. Feshali, M. Paniccia, K. J. Vahala, and J. E. Bowers, Hertz-linewidth semiconductor lasers using CMOS-ready ultra-high-Q microresonators, Nat. Photonics **15**, 346 (2021).

[85] E. Abbasgholinejad, D. Malz, A. Asenjo-Garcia, and R. Trivedi, Theory of quantum-enhanced interferometry with general Markovian light sources, arXiv:2504.05111.

[86] G. Masada, K. Miyata, A. Politi, T. Hashimoto, J. L. O'Brien, and A. Furusawa, Continuous-variable entanglement on a chip, Nat. Photonics **9**, 316 (2015).

[87] S. Shi, L. Tian, Y. Wang, Y. Zheng, C. Xie, and K. Peng, Demonstration of channel multiplexing quantum communication exploiting entangled sideband modes, Phys. Rev. Lett. **125**, 070502 (2020).

[88] M. Erhard, M. Krenn, and A. Zeilinger, Advances in high-dimensional quantum entanglement, Nat. Rev. Phys. **2**, 365 (2020).

[89] M. Kues, C. Reimer, J. M. Lukens, W. J. Munro, A. M. Weiner, D. J. Moss, and R. Morandotti, Quantum optical microcombs, Nat. Photonics **13**, 170 (2019).

[90] S. W. Golomb, in *Graph Theory and Computing*, edited by R. C. Read (Academic Press, New York, 1972), p. 23.

[91] M. Reck, A. Zeilinger, H. J. Bernstein, and P. Bertani, Experimental realization of any discrete unitary operator, Phys. Rev. Lett. **73**, 58 (1994).

[92] W. G. Cochran, The distribution of quadratic forms in a normal system, with applications to the analysis of covariance, Math. Proc. Cambridge Philos. Soc. **30**, 178 (1934).

[93] C. Jin, R. Ge, P. Netrapalli, S. M. Kakade, and M. I. Jordan, How to escape saddle points efficiently, arXiv:1703.00887.

[94] S. Blanes, F. Casas, J. A. Oteo, and J. Ros, The Magnus expansion and some of its applications, Phys. Rep. **470**, 151 (2009).